Investigating fracture propagation characteristics in shale using sc-CO$_2$ and water with the aid of X-ray Computed Tomography

Talal Al Shafloot, Tae Wook Kim, Anthony R. Kovscek [*]

Energy Resources Engineering, Stanford University, USA

ARTICLE INFO

ABSTRACT

The further development of unconventional resources is anticipated to increase the intensity of hydraulic fracturing operations. Injecting water-based fracturing fluids into shale formations, especially shales producing gas, may have adverse impacts of water blocking, scale formation, and water-sensitive clay minerals. Accordingly, nonaqueous candidates such as carbon dioxide (CO$_2$) need to be explored to avoid injection of millions of gallons of water and to increase the effectiveness of stimulation jobs. This study investigates fracturing behavior accompanying supercritical carbon dioxide (sc-CO$_2$) injection compared to water. A High Pressure High Temperature (HPHT) triaxial cell was utilized to conduct shale breakdown experiments under reservoir-like conditions. Furthermore, the experimental setup allows continuous monitoring of in situ details using X-ray Computed Tomography (CT). Here, CT images were utilized for the first time to investigate and confirm the breakdown pressure using Fast Iterative Digital Volume Correlation (FIDVC) that permits visualization of in situ deformation and strain. One inch diameter Green River shale samples were fractured under triaxial stress conditions. Results demonstrated a roughly 2 to 3 times greater breakdown pressure for sc-CO$_2$ compared to water for the samples studied. Compressive infiltration stress might explain such behavior, and mineralogy is believed to be a major contributor to such differences between injectants. Under isotropic horizontal stresses, sc-CO$_2$ induces fractures propagating almost independent of bedding planes. This is a promising finding for probable larger stimulated volume achieved by sc-CO$_2$. CT imaging to monitor fracture propagation demonstrated excellent performance in detecting fracture propagation. We anticipate this technique to help significantly when monitoring fracture propagation mechanisms for laboratory samples with slow pressurization as well as studies of slip on pre-existing fractures.

1. Introduction

Multistage hydraulic fracturing is commonly implemented in shale formations to enhance productivity in the wellbore vicinity. Aqueous fracturing fluids include water, foam, and acid based fluids mixed with chemicals such as surfactants and emulsifiers. Injection of water into tight unconventional formations leads to shortcomings such as liquid trapping, scale formation, and the sensitivity of shale components to water-based fluids that may result in clay swelling and dispersion (Jew et al., 2017; Gandossi et al., 2013; Shainberg et al., 1984). Furthermore, millions of gallons of water are pumped in multistage hydraulic fracturing jobs to complete a single well (Jackson et al., 2014).

To avoid slick-water associated issues, waterless fracturing was introduced for rapid cleanup of the wellbore region and potential economic advantage that might result if long-term productivity enhance-ments are achieved relative to conventional aqueous fracturing fluids. Injecting supercritical carbon dioxide (sc-CO$_2$) is the most common waterless fracturing technique showing several advantages over other candidates. Recall that supercritical means that both pressure and temperature are greater than the fluid critical point. sc-CO$_2$ is used for both enhanced oil recovery and fracturing applications (Yu et al., 2015; Rogala et al., 2013). The physical properties including small viscosity and large density qualifies sc-CO$_2$ as an excellent agent for these applications. In addition, experimentally demonstrated larger adsorption capacity to shale formations (Aljamaan et al., 2017) is anticipated to free adsorbed methane in the wellbore vicinity. However, utilization of carbon dioxide as a fracturing fluid is currently limited due to the lack of full understanding of sc-CO$_2$ interaction with shale. Moreover, multiple challenges associated with transport of CO$_2$ to the wellhead, storage, proppant transport capability, and treatment costs are expected (Zhang

---

et al., 2017).

Investigating the performance of sc-CO_2 requires examining three factors: breakdown pressure, fracture propagation direction, and induced fracture complexity. Breakdown pressure is an important parameter to estimate because of its importance in fracturing job design and economic analysis, because it provides an upper bound of maximum injection pressure in the field. Accurate breakdown pressure estimation is essential for calculating the injected fluid volume and finding the desired zones to fracture. Furthermore, understanding sc-CO_2 breakdown pressure behavior helps in predicting the potential of fracturing the seal atop conventional formations during CO_2 sequestration. Clearly, sc-CO_2 would demonstrate superiority over water for hydraulic fracturing if it exhibits smaller breakdown pressure because this will require less injected fluid and reduced pumping requirements. Moreover, an excellent candidate induces complex fractures that increase the stimulated volume. In field applications, the optimum injectant for fracturing should be economically promising and lead to minimal material and energy demands.

One way of estimating breakdown pressure is using literature-presented equations such as classical breakdown pressure for impermeable rocks (Hubbert and Willis, 1972) and for permeable rocks (Haimson et al., 1967), and fracture mechanics based models (Abou--Sayed et al., 1978; Rummel, 1987; Gdoutos, 2012). Nevertheless, none of these models fully explain breakdown phenomena and none of these models are generally accepted for this purpose (Guo et al., 1993). In addition, most fracture propagation models assume the propagation of one main fracture in the orthogonal direction to minimum stress. Such an assumption does not satisfactorily describe observed complex fractures in the experimental work to be discussed. Another way of estimating breakdown pressure is fracturing formation core samples subjected to reservoir-like stress configuration in the laboratory. Laboratory tests reveal valuable insights about expected breakdown pressure in the field under controlled conditions.

Several experimental studies investigated the performance of CO_2 as a fracturing fluid compared to water. Comparing breakdown pressure measurements for these two fluids revealed different outcomes. Some studies observed larger breakdown pressure for samples fractured with CO_2 (Alpern et al., 2012; Li et al., 2016; Jiang et al., 2018), where gaseous CO_2, liquid CO_2, and sc-CO_2 were injected, respectively. Another study demonstrated no difference in breakdown pressure between samples tested with sc-CO_2 and water (Chen et al., 2019). Finally, several studies reported smaller breakdown pressure when fracturing with sc-CO_2 (Stanisławek et al., 2017; Kizaki et al., 2012; Zou et al., 2018).

Experimentally induced fractures also behaved differently in literature studies. While a planar main fracture is the result of hydraulic fractures for almost all studies, fracturing with CO_2 generated a variety of fracture geometries. Some studies observed complex fractures with sc-CO_2 (Stanisławek et al., 2017; Kizaki et al., 2012; Zou et al., 2018; Chen et al., 2019), while others reported a planar main bi-wing fractures (Zhang et al., 2019; Li et al., 2016). The lack of agreement among breakdown pressure magniteues for CO_2 and water necessities the need for further investigation of sc-CO_2 performance as a fracturing fluid. Additionally, understanding fracture propagation behavior induced by sc-CO_2 is a major area of interest.

A thorough experimental investigation of fracturing behavior during sc-CO_2 utilization requires satisfying criteria to reveal meaningful data. Experiments should be conducted in reservoir-like conditions such as stress configuration, temperature, injection pressure, and pore pressure. When comparing the performance of different fluids, testing under similar conditions is essential. In addition, continuous monitoring of tested samples assists in capturing the breakdown pressure moment and, possibly, fracture evolution. Injecting CO_2 in the supercritical state is essential to capture the effect of phase behavior on fracture characteristics. Nevertheless, many experimental studies in the literature fail to meet one or more of these aspects for a variety reasons. Building an

experimental setup that is safe to conduct tests in reservoir-like conditions is difficult. Even if similar to in-situ conditions were applied, monitoring the fracturing process in situ using, for instance, x-rays is restricted by the dense material used to ensure safe experiments. Interestingly, most studies conducted experiments under similar flow-rate conditions and not similar pressurization rates. Another important issue is that most experimental studies use sharp upstream pressure drop or acoustic emissions (AE) to interpret breakdown pressure. However, both of these measures are indirect indications of the breakdown pressure moment. Finally, a small number of experiments were conducted on rock samples using CO_2 in the supercritical state, as outlined above.

Accordingly, we investigate fracture propagation mechanisms in Green River shale accompanying sc-CO_2 and water injection fulfilling to the greatest extent the criteria mentioned above. An X-ray Computed Tomography (CT) setup with triaxial-stress capabilities was prepared to conduct fracturing experiments for shale samples using sc-CO_2 and water. We studied the breakdown pressure behavior and the structure of fractures induced by both fluids. CT imaging, with appropriate fast digital image volume correlation (FIDVC), was used to interpret stress in situ and to monitor fracture propagation.

2. Methodology

This section describes the CT-scannable experimental apparatus, the shale samples, sample preparation, and the experimental procedure. CT scanning of unconventional rocks provides important in situ details, e.g. Vega et al. (2014).

2.1. Experimental setup

A schematic of the experimental setup is illustrated in Fig. 1. The HPHT cell is enlarged for better visualization of its interior structure. This novel cell was designed by Glatz et al. (2018), and it can accommodate temperatures of at least 400 °C, confining pressure of 13.8 MPa, and 68.9 MPa axial load. The sample is installed in the middle of the pressure cell and connected to upstream and downstream fluid delivery and production. Pressure is monitored using a transducer (Model:PTX 1400) $\pm$ %0.15 accuracy. The upstream line is connected to an accumulator that helps pressurize sc-CO_2 using a Teledyne 500D ISCO pump. A heater and temperature controller maintains the apparatus temperature such that carbon dioxide is in the supercritical state (31.0° C). In case of water fracturing, water is injected directly using an ISCO pump. The sample is jacketed to prevent communication of pore fluids with confining gaseous N_2. Nitrogen is used as confining pressure for easier cleanup and most importantly minimal X-ray attenuation during CT scanning. The actuator is pushed towards the sample, using another ISCO pump, to apply axial load to cores. A Keyence GT2-P12K Linear Variable Differential Transducer (LVDT) is installed outside the cell on the upstream side to measure core strain by monitoring displacement. The LVDT resolution is 0.1 μm. The temperature of the accumulator and the upstream line is maintained at desired temperatures using a temperature controller. The core sample temperature is maintained using a Mica heater. Temperature is monitored using (OMEGA) thermocouples (K type) located on the sample, cell wall, upstream line, and accumulator.

2.2. Sample characterization

Green River shale core plugs were tested and used. The Green River shale basin is an enormous oil shale resource located in eastern Utah, western Colorado, and southern Wyoming (Dyni et al., 2006). The oil resources in this basin are estimated to be around 4.3 trillion barrels equivalent (Birdwell et al., 2013). The formation is categorized into two members: an upper carbonate-rich Parachute Creek and a lower clay-content rich Garden Gulch (Burnham, 2018). Geomechanical properties of the Parachute Creek member were thoroughly analyzed
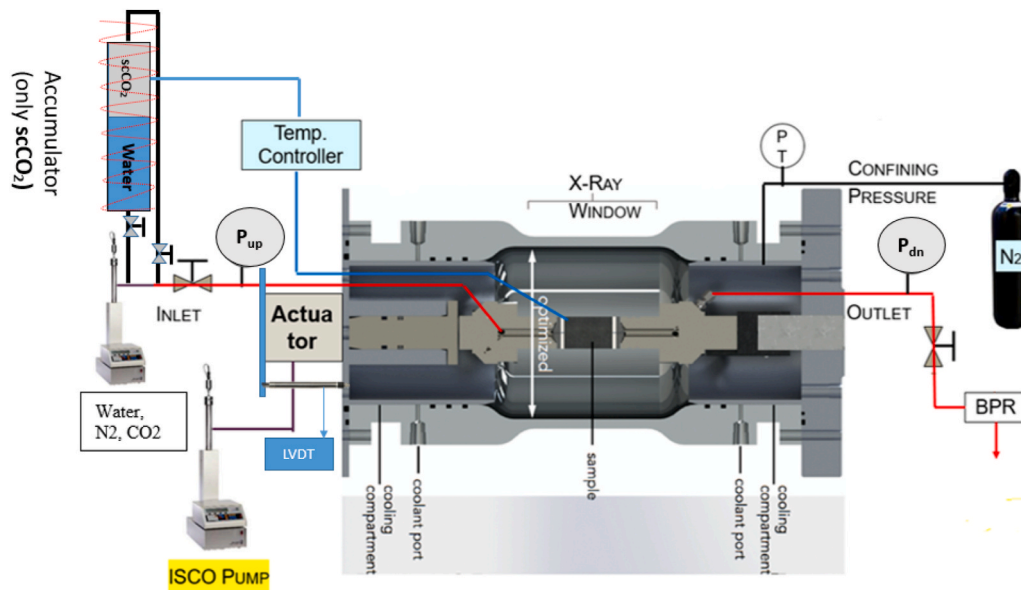
Fig. 1. Schematic of experimental setup. The main cell is modified after Glatz et al. (2018).

(Closmann et al., 1979). They reported large variability in geomechancial property measurements, that indicate a considerable variation in mineralogy. For example, at 31.0° C, tensile strength measurements range from 0.76 to 7.86 MPa (110 to 1,140 psi). However, Edelman et al. (2018) reported geomechanical properties of similar mineral composition for the available samples from the Parachute Creek member. They reported values of 113.8 MPa, 8.14 GPa for compressive strength and Young's modulus, respectively. Kim et al. (2020b) reported porosity values of several Parachute Creek member samples to range from 2.3% to 6.1%. Permeability of a horizontal sample from this member was measured to be as low as 140 nD (Kim et al., 2020a).

On the other hand, several studies investigated the geomechanical properties of the Garden Gulch member (Burnham, 2018; White et al., 2017). Burnham (2018) concluded that Garden Gulch samples demonstrated smaller Young's modulus values than Parachute Creek members, and this difference decreases as the kerogen content increases. Furthermore, measured compressive strength for several rocks demonstrated much lower values than the Parachute Creek member. These findings suggest greater ductility for the Garden Gulch member.

2.3. Sample preparation

Test samples in this study were cored horizontally, that is parallel to bedding, from different depths and locations. Cylindrical plug end faces were smoothed to insure equal distribution of load when applying axial stress. This step resulted in somewhat different sample lengths. Thereafter, a hole for injection was drilled that was 0.125 inch diameter and 1 inch long. If the core sample length was shorter than 2 inches, the length of the central borehole was decreased to half of the sample length.

Careful drilling was required to insure no introduction of defects, and the sample was scanned using a micro-CT scanner to assure a smooth borehole was drilled. Table 1 summarizes the sample information for all of the 1 inch diameter plug samples. Fig. 2 shows photographs of the core samples. This study aimed to test three pairs of samples from different depths, each pair was used for sc-CO_2 and water fracturing, respectively. However, because of limited availability of samples, two pairs were secured while the "C" pair was from the same location but different depths.

Once a sample was ready for testing, two endcaps were attached to each face. The upstream endcap has a tip that goes inside the hole bored in the center of the sample (Fig. 3a). Both endcap sidewalls contain two chemical resistant o-rings for further isolation from the confining fluid (Fig. 3b). Before applying the viton sleeve over the core sample, heat-shrinkable Teflon tubes were applied with an aluminum foil layer in between the tubes, Fig. 3c. Then, the configuration was jacketed with a Viton sleeve to secure isolation from the confining gaseous nitrogen. Finally, two metal clamps were installed on top of the O-rings. Then, the whole configuration was ready to be installed in the main HPHT cell (Fig. 3d). This method of sleeving was found to be the most successful.

2.4. Experimental procedure

The experiment started by exerting triaxial stresses on the sample. The axial stress was the largest stress ($\sigma_1 = \sigma_v$) to which the sample was subjected. It was applied through the actuator. The confining space was filled with nitrogen to exert a uniform horizontal stress ($\sigma_2 = \sigma_3 = \sigma_h$). The experiment started at a differential stress ($\sigma_1 - \sigma_2$) of 20 MPa. The confining pressure (horizontal stress) was designed based on the setup
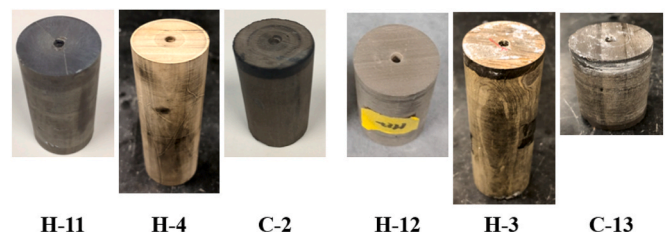
Table 1
List of samples considered for fracturing experiments.

Sample	Fluid used	Depth (m)	Dimension L (cm) * D (cm)	Bulk density (g/cm^3)
H-ll	sc-CO_2	714.5	5.1 * 2.54	2.21
H-4		148.1	7.1 * 2.54	1.97
C-2		2284.6	4.8 * 2.54	2.30
H-12	Water	714.5	4.8 * 2.54	2.21
H-3		148.0	7.1 * 2.54	2.04
C-13		3196.1	3.8 * 2.54	714.5

Fig. 2. Images of test samples: before experiment (H-4, H-12) and after experiment (H-11, C-2, H-3, C-13). Image height for each core relatively reflects sample length.
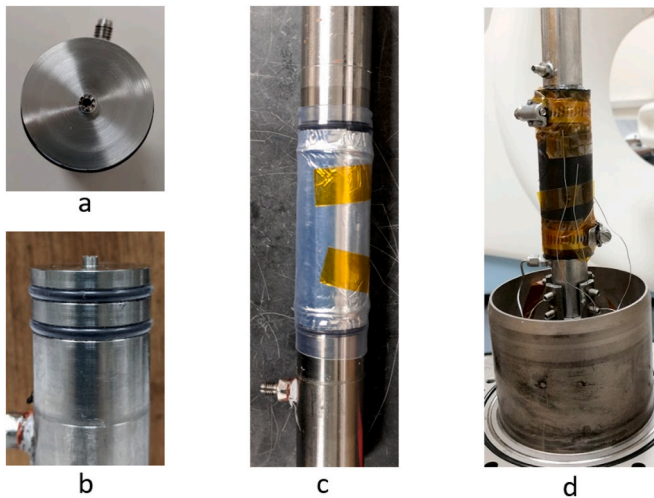
Fig. 3. Sealing technique demonstration: (a) Upstream endcap including tip for injection. (b) Endcap sidewall double O-rings. (c) layers applied before Viton sleeve. (d) Viton sleeve and clamps.

limitation and the observed values in the field (Stock et al., 1985). Thereafter, temperature was increased in the accumulator, connection lines, and the sample to approximate field conditions, above the critical temperature of CO_2.

The fracturing experiment started with injecting the fluid into the central borehole and stopped shortly after a sudden sharp drop in upstream pressure. This is the signature of breakdown pressure in the field and most experimental studies. Here, the sample was continuously scanned using a CT scanner. These scans were processed to confirm the breakdown pressure point. One method was to inspect CT images for fracture creation because fluid density (fluid that fills the fracture) is much lower than matrix density. This contrast was reflected in the CT number, and it was possible to observe a fracture. The other method was to implement FIDVC techniques to calculate strain change as illustrated by Kim et al. (2020b). Implementing these two methods to confirm the breakdown pressure point was novel. Finally, a Zeiss Xradia 520 Versa X-ray microCT was utilized to scan fractured samples to visualize the generated fracture using segmentation techniques.

CT scanning during breakdown tests was conducted using a GE HiSpeed CT scanner. The scanner was operated using a 120 mA tube current and 140 kV voltage. Scans capture a 10 cm field of view with 195 $\times$ 195 $\times$ 625 μm voxel resolution. On the other hand, a much higher resolution Zeiss Xradia 520 Versa X-ray microCT was used pre and post test to image samples at finer resolution. It was set to an optimum field of view of 28 mm that resulted in a 28 $\times$ 28 $\times$ 28 μm voxel resolution. Scans were taken with source parameters of 140 kV voltage and 0.071 mA current. Image acquisition times were on the order of hours with the Xradia scanner making it inappropriate for use during breakdown experiments.

3. Results

3.1. Breakdown pressure

Fracturing experiments with water were carried out at a 0.1 mL/min injection rate. The pressurization rate was monitored for successful tests to conduct experiments with sc-CO_2 at a similar pressurization rate. Different injection rates for the two fluids are used because the literature reports that pressurization rate influences breakdown pressure and greater loading rates resulted in greater measured breakdown pressure (Haimson et al., 1967; Zoback et al., 1977). Flowrate alone is not reported to influence breakdown pressure.

Consistent with the literature (Zou et al., 2018), a larger injection

rate was needed with sc-CO_2, as compared to water, to achieve similar pressurization rates due to greater fluid compressibility. This pressurization rate was fulfilled at a flowrate of 2.0 mL/min during the later stage of experiments. While hydraulic fracturing tests lasted an average of 20 min, fracturing with sc-CO_2 lasted more than an hour. This difference in timing was attributed to the compressibility of sc-CO_2. To have a meaningful comparison, tests were carried out at similar conditions such as confining pressure and temperature. The Supporting Information presents the pressure and injection rate histories of all tests. We were able to fracture five samples out of the six cores intended for testing. Table 2 summarizes the results obtained for all experiments.

Breakdown points were determined using the sharp pressure drop signature in addition to the CT scans. We labeled tests as successful if the test met the following criteria: signature breakdown point, confirmation of breakdown time using CT images interpreted with the FIDVC technique, as well as visible fractures observed in the post-test micro-CT scan. For successful tests, fracturing with sc-CO_2 resulted in a much larger breakdown pressures that were almost three times greater than samples fractured with water. Furthermore, for the same fracturing fluid, the values of breakdown pressures have relatively small deviations and this is indicative of experimental reproducibility. Interestingly, we could not fracture sample C-13 as a result of water injection even though a pressure of 61.4 MPa (8900 psi) was reached. This value is greater than the breakdown pressure measurements for samples fractured with sc-CO_2. Looking at the breakdown pressure magnitudes for each phase, they are relatively similar thereby confirming consistency of results. Again, C-13 demonstrated a very different behavior that requires further investigation.

3.2. Fracture structure

Segmentation of micro-CT images enabled us to visualize the fracture structure. Fig. 4 is an illustration of the fracture structure captured for samples H-11 and H-12. However, identifying the exact extension of the fracture within the core is difficult using segmentation alone. This could be attributed to the very small width of the fracture boundary that makes it difficult for automated segmentation techniques to detect. For better illustration, three slices along fractured cores are demonstrated along with fracture characteristics: near the upstream face of the sample, at the wellbore tip, and below the wellbore end (Fig. 5). For all samples, bedding direction is horizontal to have a reference to fracture propagation direction.

A general trend of bi-wing vertical fractures was observed for fractures induced by both fluids. However, only sample H-11, tested with sc-CO_2, demonstrated slight branching near the upstream side of the sample face (Figs. 4a and 5). Additionally, all fractures were fully propagated radially toward the core outer radius. As a result, this limited the further vertical extension to the percentages shown in Fig. 5. In fact, vertical extension percentage does not correlate to the fluid injected. It is worth mentioning that extension percentages are relative to the sample length. Hence, relatively small percentages are obtained for long samples.

Fractures generally propagated in the direction of laminations. Fractures induced by water strictly propagated along the interface between high density and low density material laminations. The slight deviation in both samples H-12 and H-3 is a result of nonuniform parallelism of bedding planes. On the other hand, sc-CO_2 induced fractures showed greater tendency of deviation from bedding compared to water-induced fractures. The three samples demonstrate a 10–40° deviation from bedding planes. This deviation is demonstrated in both wings of H-11 and H-4, or for a single wing as for C-2. This result is considered as an indicator of fracture propagation independent of bedding planes for sc-CO_2 injection.

Table 2
Summary of breakdown experiments.

Fluid	Sample	Confining pressure	Temperature	Pressurization rate	Breakdown Pressure	Experiment Outcome
		MPa	C	kP$_{a/s}$	MPa	
sc-CO2	H-11	13.2	45	20	37.9	Success - fracture observed
	H-4	12.9	42	23.3	44.8	Success - fracture observed
	C-2	12.9	45	23.3	43.9	Success - fracture observed
Water	H-12	12.4	44	20	14.8	Success - fracture observed
	H-3	12.6	50	27.6	14.5	Success - fracture observed
	C-13	13.4	45	-	-	Failure - Leakage happened at 8900 psi

3.3. CT imaging aid to identify breakdown

Breakdown pressure is defined as the pressure where the fracture propagates in an unstable manner. In the literature, fracture initiation pressure is expected to be equal to or smaller than breakdown pressure. As a result, breakdown pressure is of interest in the field to predict the maximum pressure and to create large fractures that increase the reservoir stimulated volume.

Reported breakdown pressure measurements in the laboratory are the largest injection pressure, assuming that unstable propagation introduces a relatively large volume that results in the consequent drop. Some methods were implemented to identify the moment of unstable fracture propagation and confirm that it matches the maximum pressure point. One method utilizes Acoustic Emission (AE) to measure the energy intensity released from the rock deformation (Chen et al., 2018). It is expected that abrupt changes in AE measurements reflect breakdown pressure. However, Chen et al. (2018) reported some drawbacks of this approach. For constant pressurization rate experiments, another approach is to detect the change in the slope of the flow rate profile over time. However, this method is sensitive to volume losses and fails for constant flow rate tests. Therefore, another approach involving visualization is needed.

CT imaging is an effective tool to visualize rock and fluid behavior during laboratory-scale fracturing processes. CT images are, typically, scans of thin sections across the core that can be analyzed individually or as a three dimensional image where data between slices are interpolated (Akin and Kovscek, 2003). Fast Iterative Digital Volume Correlation (FIDVC) is a non-invasive, iterative, and 3D technique to measure deformation (Bar-Kochba et al., 2015). The FIDVC method processes non-deformed and deformed images by wrapping them symmetrically utilizing a linearized, incremental displacement field until they reach

the same final configuration. Further details about the methodology are found in Bar-Kochba et al. (2015). In addition, implementation of this technique to serve our purposes is explained in Kim et al. (2020b). FIDVC directly calculates the displacement in situ that permits estimation of the first and second strain invariants (I_1 and I_2). We chose these parameters because the former is related to the hydrostatic aspect of the strain tensor (ε), while the latter relates to the deviatoric aspect. We used these two parameters to inspect fractures.

The volumetric strain (ε_V) represents the unit change in volume, i.e. the change in volume divided by the original volume (Upadhyaya, 2005). Volumetric strain (ε_V) is calculated as in equation (1). Assuming small strain, the equation is simplified to the sum of each strain component because the squared and cubed terms can be neglected (Ghaboussi et al., 2017).

$$\varepsilon_V = \frac{\Delta V}{V} = \frac{((x + \Delta x)(y + \Delta y)(z + \Delta z) - xyz)}{xyz}$$

$$= (1 + \varepsilon_{xx})(1 + \varepsilon_{yy})(1 + \varepsilon_{zz}) - 1$$

$$\approx \varepsilon_{xx} + \varepsilon_{yy} + \varepsilon_{zz} \tag{1}$$

where ε is the strain tensor. Note that eq. (1) is tr(ε) that is the first invariant of strain.

The second invariant of strain (I_2) reflects how much shearing deformation occurred without a change in volume, with the assumption of small strain (Lai et al., 2009; Ghaboussi et al., 2017). It is calculated using the following equation:

$$I_2 = \begin{vmatrix} \varepsilon_{yy} & \varepsilon_{yz} \\ \varepsilon_{zy} & \varepsilon_{zz} \end{vmatrix} + \begin{vmatrix} \varepsilon_{xx} & \varepsilon_{xz} \\ \varepsilon_{zx} & \varepsilon_{zz} \end{vmatrix} + \begin{vmatrix} \varepsilon_{xx} & \varepsilon_{xy} \\ \varepsilon_{yx} & \varepsilon_{yy} \end{vmatrix}$$

$$= \varepsilon_{xx}\varepsilon_{yy} + \varepsilon_{yy}\varepsilon_{zz} + \varepsilon_{xx}\varepsilon_{zz} - \varepsilon_{xy}^2 - \varepsilon_{yz}^2 - \varepsilon_{xz}^2 \tag{2}$$

To illustrate the applicability of our approach, two tests are presented. For sample H-3 that is fractured with water, we show the deformation evolution throughout the experiment to demonstrate the deformation behavior before and after breakdown. Deformation after breakdown, as evidenced by a sharp upstream pressure drop, of sample C-2 is investigated thoroughly to confirm effectiveness of our approach for sc-CO^2 fracturing experiments. Table 3 shows both experimental conditions and parameters of the FIDVC method for these two experiments. The temperature and pressure conditions for sc-CO_2 case (C-2) prior and post-breakdown are almost identical. The density of sc-CO_2 is sensitive to temperature and pressure, hence we utilize scans at similar conditions. On the contrary, the effect of pressure is negligible in the case of water, due to the incompressibility of water. As a result, we were able to implement our approach to CT scans obtained at pressures of 8.8 and 13.0 MPa.

In Table 3, the correlation window is defined as the unit of the displacement field given by the Gaussian function of 64 voxels width. The minimum number of voxels in any dimension should be 1.5 times the correlation window. Because the z-direction of sample C-2 has the
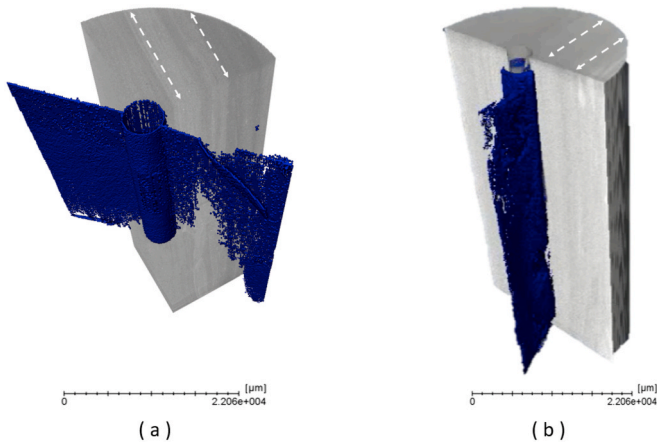
Fig. 4. Fracture structure after breakdown as obtained using thresholding th and segmentation: (a) H-11 using sc-CO_2 (b) H-12 using water. Dashed lines on the core sample indicate the bedding direction.
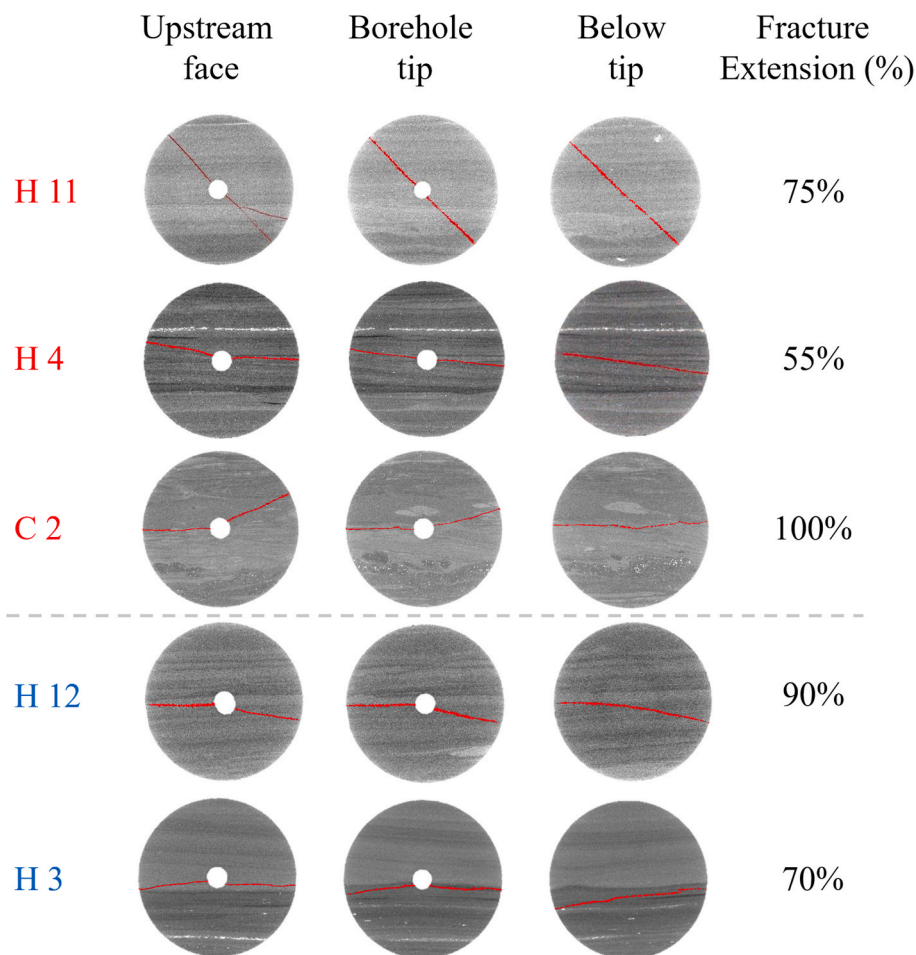
Fig. 5. Fracture geometry summary for sc-CO^2 (H-11, H-4, C-2) and water(H-12, H-3) fractured samples. Red lines mark fracture direction. Fracture extension percentage is relative to sample length.

Table 3
Experimental conditions and FIDVC parameters for illustration.

Sample	Experimental Conditions			FIDVC parameters		
	Fluid	Upstream Pressure (Mpa)	Temperature ($^\circ$C)	Correlation Window size	Display Mode (DM)	Data size (X by Y by Z)
H-3	Water	8.8–13.0	45	64 * 64 * 64	2	120 * 120 * 117
C-2	sc-CO^2	13.1	45			108 * 108 * 96

minimum of 96 voxels, we adopted 64 voxels as the correlation window in this study. The display mode represents the averaging interval for computation reduction. While assigning a value of two to display mode, the code averages every 2 meshes to reduce the computational costs. Prior and post breakdown data should be the same dimensions for reliable output.

3.3.1. Deformation evolution illustration

The pressure profile of the H3 fracturing experiment (see Supporting Information) exhibited the expected continuous increase as a constant water injection rate of 0.1 cm$_3$/min was applied, until the characteristic pressure drop happened at 2109 psi (14.5 MPa). We processed three CT scans of the core to calculate deformation before and after the break-down pressure signature. Two image stacks were scanned before the pressure drop: one at 8.8 MPa and the other at 12.1 MPa. A third scan was taken right after breakdown where pressure stabilized at a pressure magnitude that is slightly greater than confining pressure (13.0 MPa). We wanted to investigate the deformation change across breakdown pressure.

Fig. 7 represents the deformation change in XZ and YZ planes for vertical slices that intersect with the wellbore and are useful to capture fracture propagation from the wellbore. For each plane, volumetric strain (ε_V) and the square root of second invariant ($\sqrt{I_2}$) profiles are shown prior to and post breakdown. Furthermore, post breakdown CT and μ-CT scans are presented. Both CT and μ-CT images represent the same slice, and this is achieved by matching high density material that is indicated with blue arrows. The observed fracture in these two images further confirms the successful matching of the same slice. Red arrows indicate fracture propagation in both images. In CT images, blue reflects low density while the red color is an indication of high density material. The blue region extending downward from the borehole bottom is an evidence of fracture propagation. Fig. 6 illustrates the propagation of fracture right after breakdown happens. Note that deformation calculations (Fig. 7) are performed for the entire range of x- and y-planes in CT images and, similarly, for the vertical range of CT images parallel to strain invariants.

Prior to breakdown, volumetric strain (ε_V) and the the square root of second invariant ($\sqrt{I_2}$) demonstrated almost a uniform distribution for
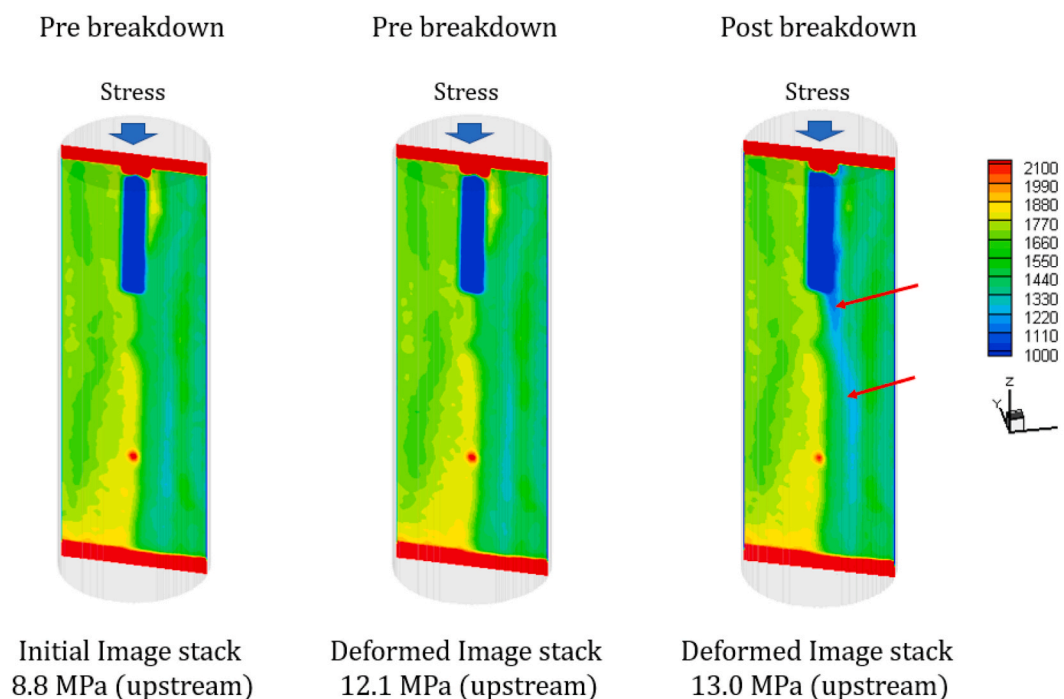
Fig. 6. Illustration of fracture visualization using CT images at increasing pressure from left to right for sample H-3. Images give raw CT number. Larger numbers indicate more dense material.

both planes (XZ and YZ). A small variation around the wellbore, dissipating toward sample edges, is attributed to the stress introduced from fluid pressurization. On the contrary, the distribution of post breakdown ε_V and $\sqrt{I_2}$ reflects major changes in their profiles. Volumetric strain (ε_V) demonstrates expansion, indicated by red color, at the fracture location observed in μ-CT images. This expansion causes a compaction zone in the vicinity of the fracture, that is the blue color bounding the red zone. In both planes, the visualized fracture in CT and μ-CT images follows the exact path of the extension zone. Second invariant of strain ($\sqrt{I_2}$) demonstrates an increase in the magnitude in the same exact direction as the visualized fracture in the post breakdown case for both planes. This behavior is not recognized in the pre-breakdown calculations, where an almost uniform distribution is observed.

Fig. 8 demonstrates the difference in ε_V and $\sqrt{I_2}$ behavior for three XY slices (50, 68, and 80) before and after breakdown. Slices were chosen to capture deformation within different segments of the sample where stress concentration might be influenced by the wellbore. As in Fig. 7, CT and μ-CT images for each slice is shown to compare deformation behavior to induced fracture. Fracture extension is captured in both CT and μ-CT images for all slices. The fracture is indicated with red arrows. Similar responses for ε_V and $\sqrt{I_2}$ in the XZ and YZ planes are also observed in the XY case. You can see a uniform distribution for pre-breakdown scans for all slices, except slice 80 that illustrates some noise attributed to the pressure exerted by the fluid on the borehole and the proximity of the upstream endcap that exerts large axial stress. On the other hand, post breakdown images reflect changes along the direction of the observed fracture in CT and μ-CT images. Volumetric strain (ε_V) indicates fracture propagation along the expansion zone, while $\sqrt{I_2}$ reflects an increase in the magnitude along the fracture propagation direction. It is important to point out that calculations of ε_V and p I$_2$ were performed on the same set of CT images. CT images are enlarged to ease the visualization of fractures.

These results demonstrate some advantages of CT imaging techniques to confirm breakdown pressure. Raw CT data visualized the fracture in sample H-3. It is not always guaranteed to recognize fractures directly from CT images because fracture width can fall below CT resolution. However, applying the FIDVC method to detect fractures

reveals strong evidence of fracture propagation. We showed how distinct features were observed for deformation analysis for scans after breakdown. In fact, the results are promising for the technique to track fracture extension for large samples when injecting reasonable flow-rates, provided that the apparatus can be scanned. Furthermore, applying this methodology might be of a big help to determine fracture initiation pressure that is smaller than or equal to breakdown pressure. This could be achieved by conducting a slow pressurization experiment to allow high frequency CT scanning because the image acquisition time is on the order of seconds and repeat scans can be conducted at roughly 4 minute intervals.

3.3.2. Deformation across breakdown point

The upstream pressure of sample C-2 declined sharply at 6374 psi (43.9 MPa) indicating breakdown. We estimated deformation between all consecutive scans prior to breakdown to inspect for fracture initiation. The reason for comparing deformation between consecutive scans is to minimize the influence of pressure increase, where larger pressure increases the density of sc-CO_2 and consequently the CT number. We did not detect any induced fracture before the pressure drops. Because the upstream pressure dropped to the confining pressure, we calculated deformation using the scan taken at the confining pressure magnitude prior to the breakdown moment (13.1 MPa). Fig. 9 illustrates the deformation in XZ and XY planes. For each plane, volumetric strain (ε_V), square root on second invariant ($\sqrt{I_2}$), CT scan and μ-CT image post breakdown are presented. Large density materials, indicated with blue arrows in both scans, are matched in CT and μ-CT. In Fig. 9, deformation calculations for XZ and XY planes are for the identical range of CT images shown.

In Fig. 9a, the post breakdown CT image does not indicate fracture extension, attributed to the fracture width falling below CT imaging resolution. Nevertheless, volumetric strain (ε_V) and square root of second invariant ($\sqrt{I_2}$) reveal that a fracture was induced. The ε_V maximum values are concentrated at the wellbore region as an impact of an increase in axial stress between the two scans used to generate deformation profiles. The fracture influence is reflected at the bottom of the image where the fracture matches the expansion zone. This is the same
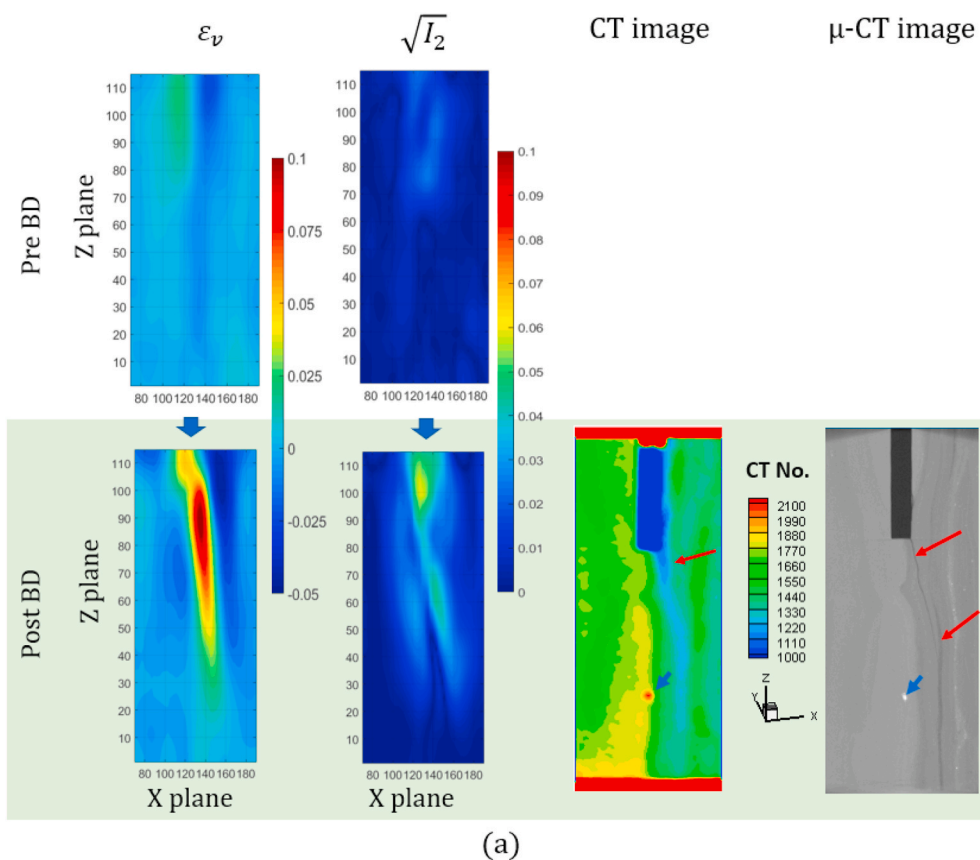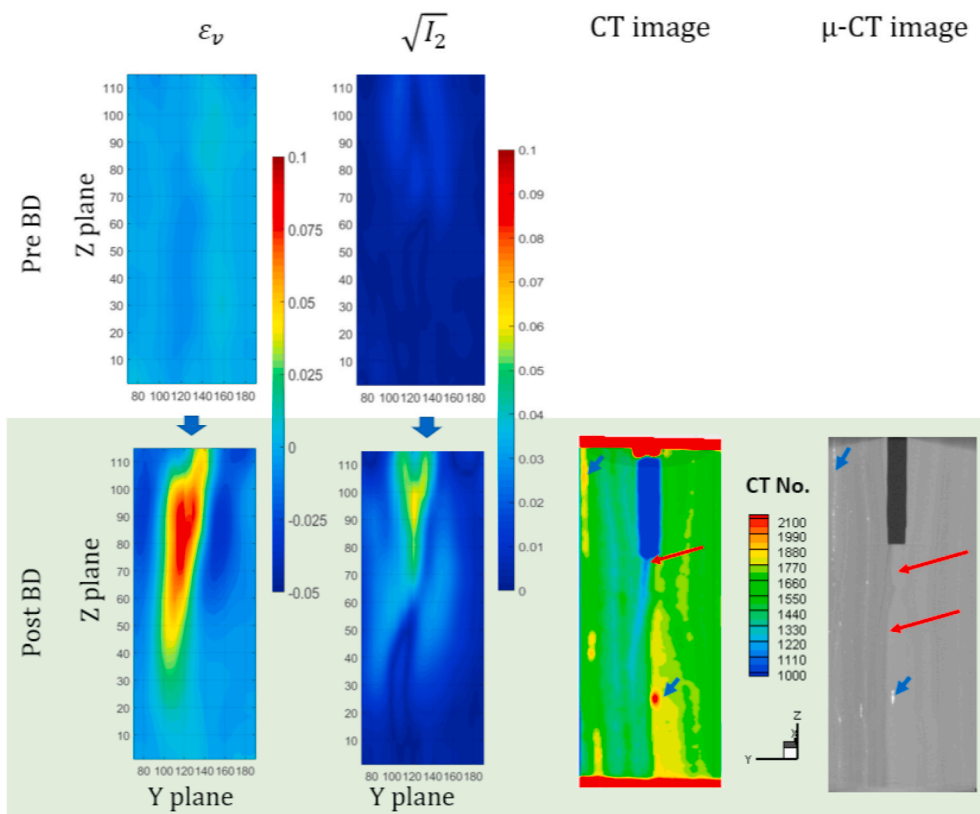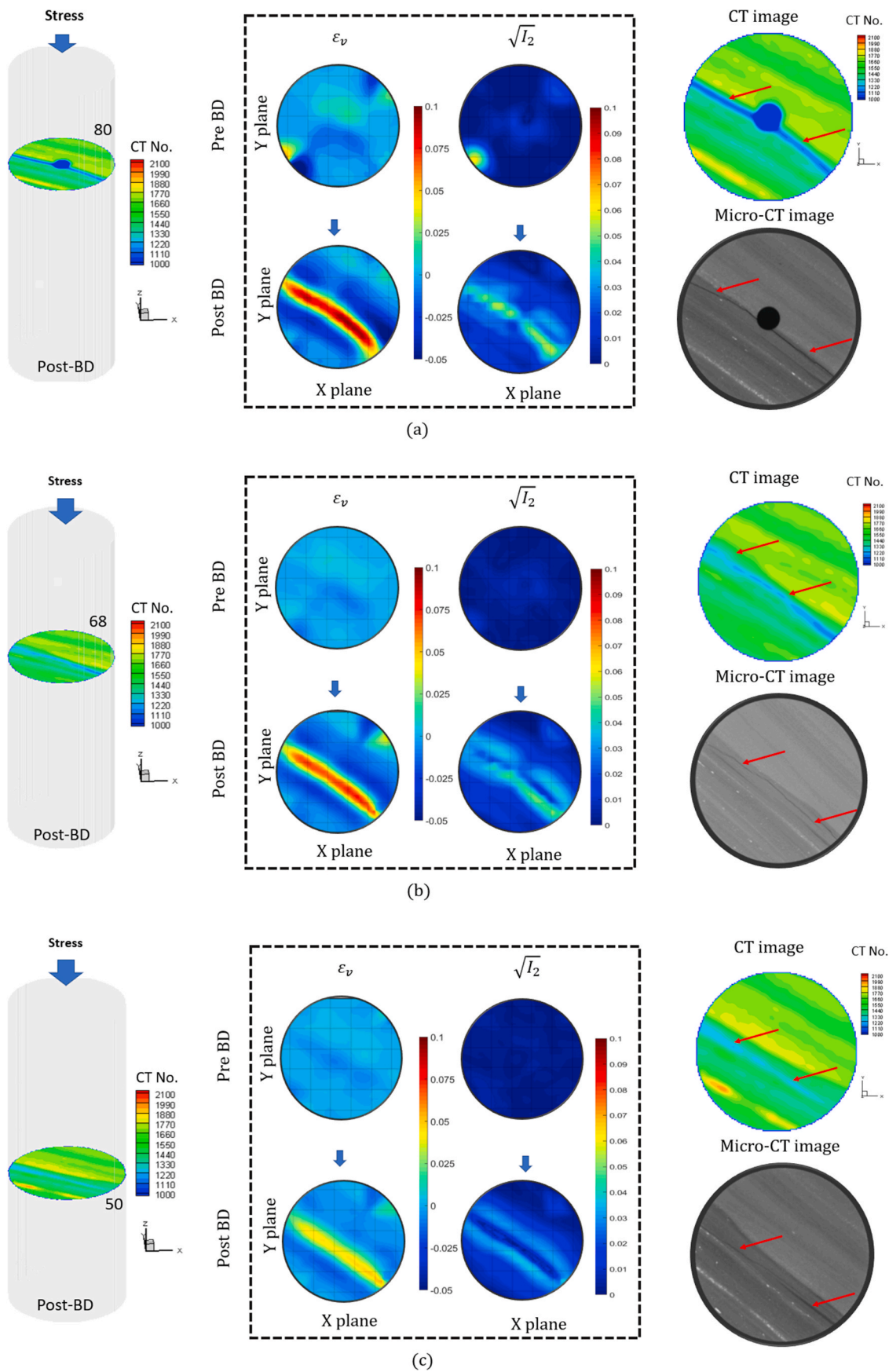
Fig. 7. The distribution of ε_V and $\sqrt{I_2}$, as obtained from FIDVC, on (a) XZ and (b) YZ plane with μ-CT image and X-ray CT images post breakdown for sample H-3. The range of ε_V is from −0.05 to 0.1. $\sqrt{I_2}$ ranges from 0 to 0.1. For figures generated using the FIDVC technique, a unit is equivalent to 195 μm and 625 μm in the x-axis (X and Y-planes) and y-axes (Z-plane), respectively.

Fig. 8. The distribution of ε_V and $\sqrt{I_2}$ on XY plane (a) slice 80 (b) slice 68 (c) slice 50 plane with μ-CT image and X-ray CT image post breakdown for sample H-3. The range of ε_V is from -0.05 to 0.1. $\sqrt{I_2}$ ranges from 0 to 0.1. The diameter of the images generated with the FIDVC technique is 22.7 mm.
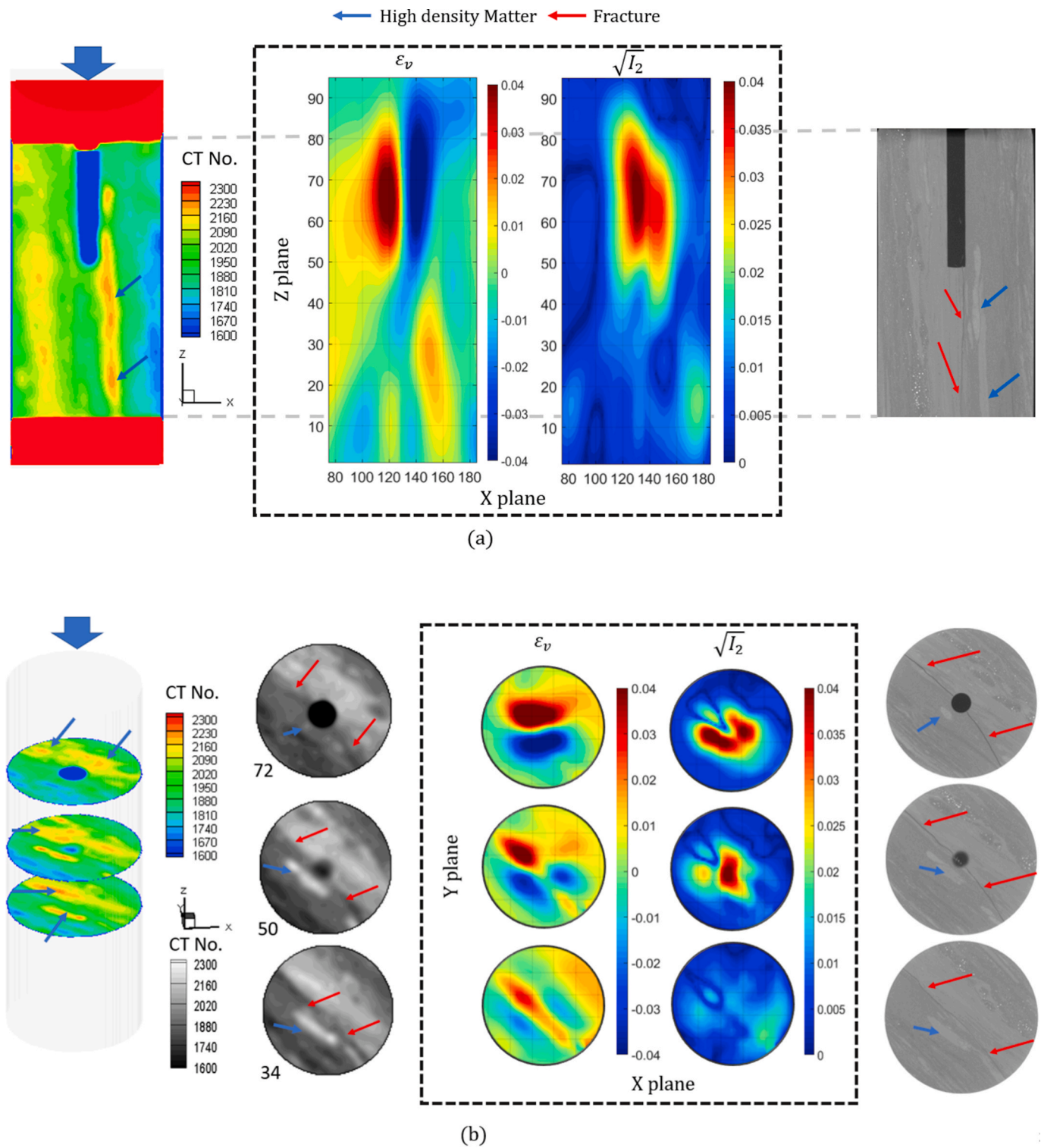
Fig. 9. The distribution of ε_V and $\sqrt{I_2}$ in the XZ plane for sample C-2, with μ-CT and CT images post breakdown for sample C-2. The range of ε_V is from −0.04 to 0.04. $\sqrt{I_2}$ ranges from 0 to 0.04. For the XZ plane, a unit in the FIDVC figures is equivalent to 195 μm and 625 μm in the x and y axes, respectively. XY plane images has a diameter of 22.7 mm.

behavior observed for sample H-3 discussed previously. Second invariant ($\sqrt{I_2}$) showed a slight increase in the magnitude at the matching fracture location in the μ-CT image. For both parameters, the smaller change in magnitude after fracture propagation supports smaller induced fractures than those in sample H-3. The noise in the XZ plane strains is attributed to the increase in differential stress between original and deformed scans. Nevertheless, we were able to visualize the fracture and the noise dissipates as we move away from upstream endcap.

In XY slices (Fig. 9b), we were able to observe a fracture in CT images by zooming and applying a proper threshold. The ε_V values at slice 72 are greatly distorted by the axial load increase that is amplified by the borehole effect in altering stress distribution. However, this negative

impact dissipates as the scan is further from the upstream endcap. Slices 34 and 50 demonstrate the expansion zone bounded by compression, that matches the fracture observed in the μ-CT image. The $\sqrt{I_2}$ profile reflects the same distortion at slice 72 that declines as we move down the core. However, the magnitude increases in the direction of the fracture for all slices, especially for the left wing of the fracture.

Results from our analysis demonstrate the advantage of utilizing CT images to identify the fracture propagation moment in fracturing experiments for different fluids. Raw data from CT scans reveal the fracture introduction in a majority of the cases. Visualizing results from different planes with a proper threshold increases the chance of detecting fractures. FIDVC implementation illustrates excellent performance in detecting fractures in all tests. Volumetric strain (ε_V) and square root of second strain invariant ($\sqrt{I_2}$) calculated from deformation reveal clear indications of fractures being induced. For all experiments in this study, breakdown pressure is confirmed to be the pressure where the upstream pressure profile experiences a signature sharp drop. This is supporting evidence of the validity of assuming unstable fracture propagation at the point where pressure drops.

4. Discussion

4.1. Breakdown pressure

The breakdown pressure measurements in our experiments reveal that sc-CO₂ fracturing requires larger pressure than water. Although water is injected, C-13 demonstrated resistance to fracturing up to a pressure of 8900 psi (61.4 MPa), that is greater than the breakdown pressures recorded for sc-CO₂. Li et al. (2016) fractured Green River shale samples using l-CO₂, g-N₂ and water. They utilized similar sample sizes as our study, cylindrical 2 inch length and 1 inch diameter, and introduced similar borehole dimensions. Our results are plotted along with their results for illustration and further investigation (Fig. 10). Results from Li et al. (2016) demonstrated larger breakdown pressure for sc-CO₂ compared to water. Nevertheless, the difference they reported was not as large as our results. We recorded as large as three times the breakdown pressure of water-fractured plugs.

Fracturing with water resulted in breakdown pressure measurements that are several hundreds of psi greater than the confining pressure. These measurements agree with the fact that the fracture needs to overcome the minimum stress in order to propagate perpendicular to it. Several studies reported such behavior of breakdown pressure correlating with minimum stress with a factor of one ($P_b = \sigma_3 + constant$) (Guo et al., 1993). However, sample C-13 did not behave similar to the other two samples fractured with water. The expected reason behind such behavior is the significant mineralogy difference between C-13 and all other samples. X-ray diffraction (XRD) results reveal that C-13 belongs to the Garden Gulch member, while the other samples were cored
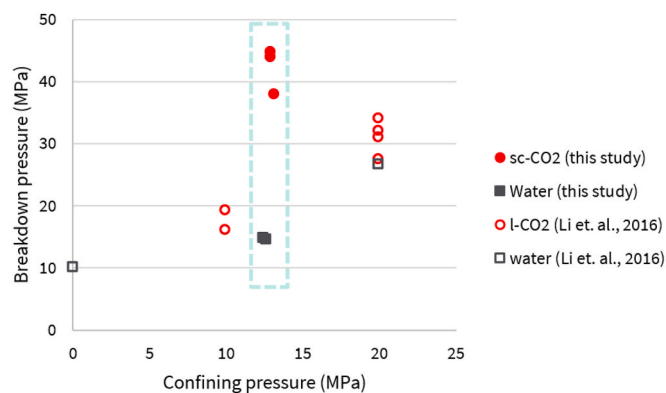

Fig. 10. Breakdown pressure as a function of confining pressure including results from this study (filled symbols) and from Li et al. (2016) (open symbols).
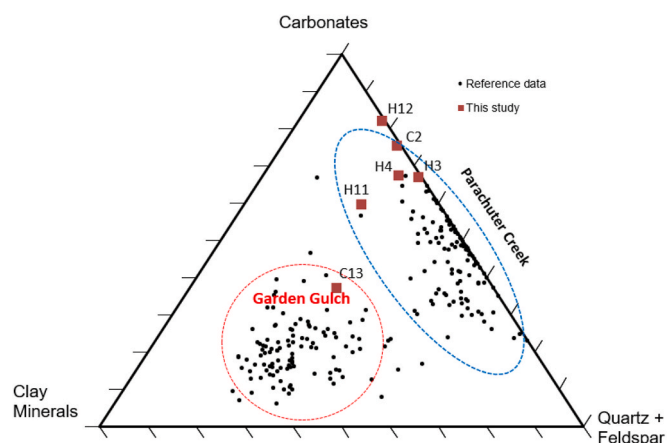

Fig. 11. Mineral composition of samples tested in this study. Image modified from the original of Burnham and McConaghy (2014).

from the Parachute Creek member (Fig. 11). The depth where sample C-13 is cored, compared to the remaining samples, supports that it belongs to this member (Table 1). As illustrated in Fig. 11, the Garden Gulch member is known for its very high clay-content. Field-scale practices show that large clay-content ductile shale formations exhibit greater breakdown pressures (Wang, 2015). Furthermore, Burnham (2018) reported substantially lower Young's modulus values for Garden Gulch than Parachute Creek. This is an indication of ductility, reported in the literature to resist fracture initiation, and hence, requires much larger pressure to initiate a crack (Bai, 2016).

In the case of sc-CO₂ injection, The need for larger pressure to induce a fracture in an unstable manner (breakdown pressure) is attributed to several factors. The unique properties of low viscosity and almost zero interfacial tension enables sc-CO₂ to penetrate into the matrix, even in the case of very low permeability. This leak-off results in pressure buildup in the matrix and pressurizing the wellbore in a less sufficient manner. Pressure models using loss of circulation theory indicate that pressure buildup in the matrix increases the total stress and prevents fracture propagation (Morita et al., 1990). Moreover, this infiltration induces compressive infiltration stress at the wellbore wall requiring extra pressure to overcome (Lubinski, 1954). This compressive infiltration stress is proportional to the difference between pressure at the wellbore and pore pressure. Starting the experiments with a zero pore pressure is expected to cause this stress to be more pronounced. Larger compressiblity transfers the pressure load from wellbore to the fracture tip in a slower and much less sufficient manner that does not encourage the propagation process (Tomac and Gutierrez, 2017). Subsequently, we expect greater pressure is needed to reduce the impact of greater compressiblity and pressurize the fracture efficiently. Tomac and Gutierrez (2017) revealed their conclusion with the aid of a discrete element method (DEM) simulation model for quasi-brittle rocks.

Compared to sc-CO₂ breakdown pressure measurements in Li et al. (2016), our larger magnitudes are attributed to the following factors. The wide variability in mineralogy (Fig. 11) leads to variability of geomechanical properties, such as Young's modulus and Poisson's ratio, impacting the breakdown pressure significantly. For instance, Petrie et al. (2014) reported variation of cap-rock formations response to pore-fluid factor ($\lambda_v = P_f / \sigma_v$). For the same λ_v, some formations experience hydraulic extension or extensional shear while others do not. They justified this with the role of mineralogy in controlling the mechanical failure mode. Cheng et al. (2020) also emphasized that mechanical properties of rocks significantly impact fluid stimulation results. Another factor is injecting different phases of CO₂, that is expected to result in different outcomes. While liquid CO₂ is injected in Li et al. (2016), we utilized CO₂ in our experiments that is less viscous and more compressible. This difference in physical properties makes the

previously discussed effects of viscosity and compressibility more pronounced, resulting in even larger breakdown pressures. It is quite interesting that different breakdown pressure measurements were obtained for samples with similar sample dimensions from the same formation. Differences in sample composition and distribution of minerals produced considerably different results.

The interaction between sc-CO_2 and shale may play a role in the results of this study. Huang et al. (2019) investigated the change in pore structure of crushed shale samples as a result of sc-CO_2 injection at different times. As a result of CO_2 adsorption, the total pore volume decreased by approximately 20%. Most importantly, pores in the range of 0.85-2 nm decreased by roughly 50% within half an hour of saturation. This decrease in pore volume was explained using three processes, with physiosorption of CO_2 in organic matter (kerogen) being the most important process. This adsorption into kerogen results in a plasticising effect that causes expansion (swelling), and subsequently blocks both micro and nano-pores. This phenomena might contribute to the observations in this study.

Calculations reported elsewhere indicate that sc-CO_2 penetrates about 6 to 7 mm outward from the wellbore in 2 hours under conditions representative of our tests (Al Shafloot, 2021). The reduction in permeability, as a result of pore volume reduction, and the change of mechanical properties, as a result of viscoplasticity, are factors that explain larger breakdown pressures for samples fractured with sc-CO_2. Furthermore, these factors are anticipated to be more pronounced when CO_2 is injected in the supercritical state because of easier penetration into smaller pores compared to liquid. This difference might explain the larger CO_2 breakdown pressures compared to water (Li et al., 2016). Regardless of the cumulative impact of the shortterm interaction of sc-CO_2 and water with shale, the subsequent change in mechanical properties of shale, and fluid properties on fracture initiation should be further explored. It is worth mentioning that swelling and change of mechanical properties (increasing ductility) of shale samples, as a result of long-term sc-CO_2 saturation, is suggested in some studies (Lu et al., 2016) and (Lyu et al., 2018), respectively.

4.2. Fracture structure

Vertical fractures are expected to result from our experiments. Because axial stress is the largest (σ_1), the fracture is anticipated to propagate perpendicular to the minimum horizontal stress (σ_3). Elastic theory reveals that fractures propagate in the maximum compressive stress direction. Because our setup provides a uniform horizontal stress ($\sigma_2 = \sigma_3$), we expect a uniform compressive strength on the wellbore face. Subsequently, fracture propagation is controlled by other factors. Physical characteristics and rock heterogeneity are expected to be the major keys of the fracture initiation point. Weak interfaces between laminations are the most probable fracture initiation point. As a matter of fact, fractures generated in our study initiated from the wellbore side with lamination. This is demonstrated from the initiation point of less than 40° angle from lamination (Fig. 5).

Fracture extension direction depends on the injected fluid in our experiments. Fractures induced by injecting water propagated parallel to bedding because of the nature of water and samples tested. The greater water viscosity, along with the very low sample permeability, restricted water from penetrating into the matrix or small defects. Instead, water pressurizes in the wellbore until it reaches a sufficient pressure to initiate the fracture at the weakest point. Because lamination interfaces are anticipated to be the weakest planes, the fracture propagates in that direction. Germanovich et al. (1997) highlighted the preference of fractures to propagate along the layers in layered systems. Stanisławek et al. (2017) and Bennour et al. (2015) reported similar behavior of a single planar fracture parallel to bedding. On the other hand, sc-CO_2 penetrates the matrix and small cracks prior to fracture initiation. Once a fracture initiates, it propagates through previously filled and pressurized cracks and defects. It is possible for the fracture to

propagate parallel to bedding planes because the lamination interface is also a weak spot.

These conjectures explain fracture propagation that is less dependent on bedding for sc-CO_2 treated samples as compared to water. This is illustrated by the deviation of the fracture, both wings or a single wing, by 10–40 ° angle from the bedding planes. Two studies reported generally similar behavior for sc-CO^2 induced fractures. Jiang et al. (2018) observed a random initiation point and propagation direction of fractures along weak planes or preexisting cracks for shale samples. Furthermore, similar inclination from bedding (around 30°) is reported for shale samples fractured with l-CO_2 (Bennour et al., 2015). They justified such behavior with sensitivity to small defects because of the ability of l-CO_2 to fill tiny spaces and cracks. In addition, they speculated CO_2 expansion at breakdown to be a contributing factor. There is no exact explanation justifying the degree inclination range. However, Culp (2014) investigated the influence of CO_2 on fracture complexity. He concluded an influence on fracture propagation by the fracture initiation point, breakdown pressure, and the characteristics of the fractured sample. The influence of laminations on the fracture initiation point might be a justification for such observations.

Fracture complexity observed in the CO_2 injection experiments (Zhang et al., 2017 Kizaki et al., 2012; Zou et al., 2018) could not be captured fully in our study. Only sample H-11 generated a fracture that exhibits slight branching. Evolving complex non-planar fractures are possible due to several reasons such as rock heterogeneity, stress heterogeneity, intersection with natural fractures, instability of crack extension, fracture geometry, unfavorable fracture initiation orientation, and influence of neighboring fractures (Germanovich et al., 1997; Wang, 2015). In our case, high resolution μ-CT scans do not reveal natural fractures or cracks for rock samples prior to experiments. As a result, our observations demonstrate the role of pre-existing cracks and natural fractures on enhancing the performance of sc-CO_2 to create complex fracture network. One possible reason for not capturing greater fracture complexity is the small sample size.

The observed independence of fracture extension direction to bedding while injecting sc-CO_2 is promising. Such behavior increases the possibility of connecting natural fractures. In addition, the propagation along lamination interfaces demonstrates a potential of unstable fractures that cross bedding and branch to parallel to bedding fractures. Furthermore, the observed case of slight branching illustrates the sensitivity of sc-CO_2 induced fractures to defects. All these factors are in the favor of exploiting sc-CO_2 as a fracturing agent.

5. Conclusions

This paper presented the results of fracturing tests of Green River Shale samples using sc-CO_2 and water. Breakdown pressure measurements reveal much greater breakdown pressure magnitudes resulting from sc-CO_2 injection for these samples. Successful tests revealed a breakdown pressure range of 37.9 to 44.8 MPa for sc-CO_2 injectant, while breakdown pressure is 14.5-14.8 MPa in the case of water. Our results emphasize the interaction of mineralogy and the type of hydraulic fracturing fluid. This effect is not considered in most fracturing experiments in the literature. Our study suggests testing samples with similar mineral composition and mechanical properties for meaningful results. The greater breakdown pressures associated with sc-CO_2 do not discourage usage for stimulation jobs. Other factors such as productivity enhancement, economic analysis, and environmental aspects should be considered.

The injection of sc-CO_2 induced fractures that demonstrated greater tendency to propagate independent of bedding plane directions. This independence is anticipated to generate complex fracture networks by bifurcation to parallel to bedding fractures or connecting pre-existing parallel fractures to bedding cracks. Testing samples with no preexisting cracks resulted in the observed limited fracture complexity.

Importantly, our results, in agreement with several studies in the literature, anticipate a larger stimulated volume when sc-CO₂ is used as a stimulation agent.

CT imaging of fracturing experiments illustrated an excellent performance to monitor fracture extension. Imaging captured fracture propagation under reservoir-like conditions. Raw CT images revealed and allowed identification of fractures in several cases. FIDVC was implemented for the first time in connection with breakdown pressure tests. The in situ strain, that was calculated directly from in situ deformation, indicated precise fracture propagation direction. Implementing CT scanning with FIDVC image processing is very promising to monitor fracture propagation during slow pressurization experiments to understand fracture initiation and the extension of pre-existing fractures.

Declaration of competing interest

The authors declare that they have no known competing financial interests or personal relationships that could have appeared to influence the work reported in this paper.

Appendix B. Supplementary data

Supplementary data related to this article can be found at https://doi.org/10.1016/j.jngse.2020.103736.

Nomenclature

λ_v	Pore-fluid facto
σ_1	Maximum stress
σ_2	Intermediate stress
σ_3	Minimum stress
σ_h	Minimum horizontal stress
σ_v	Vertical stress
ε_V	Volumetric strain
I_2	Second invariant of strain
P_b	Breakdown pressure
P_f	Pore pressure
V	Volume

Author contribution

Talal Alshafloot: Experiments, Investigation, Writing – original draft. Tae Wook Kim: Investigation, Visualization, Writing – original draft. Anthony R. Kovscek: Conceptualization, Supervision, Writing – review & editing.

References

Abou-Sayed, A., Brechtel, C., Clifton, R., 1978. In situ stress determination by hydrofracturing: a fracture mechanics approach. J. Geophys. Res.: Solid Earth 83 (B6), 2851–2862.

Akin, S., Kovscek, A., 2003. Computed tomography in petroleum engineering research. Geological Society, London, Special Publications 215 (1), 23–38.

Aljamaan, H., Ross, C.M., Kovscek, A.R., et al., 2017. Multiscale imaging of gas storage in shales. SPE J. 22 (6), 1–760.

Alpern, J., Marone, C., Elsworth, D., Belmonte, A., Connelly, P., et al., 2012. Exploring the physicochemical processes that govern hydraulic fracture through laboratory experiments. In: 46th US Rock Mechanics/Geomechanics Symposium. American Rock Mechanics Association.

Al Shafloot, Talal, 2021. Investigating the Performance of Supercritical Carbon Dioxide as a Stimulation Agent in Shale. PhD Thesis. Stanford University.

Bai, M., 2016. Why are brittleness and fracability not equivalent in designing hydraulic fracturing in tight shale gas reservoirs. Petroleum 2 (1), 1–19.

Bar-Kochba, E., Toyjanova, J., Andrews, E., Kim, K.-S., Franck, C., 2015. A fast iterative digital volume correlation algorithm for large deformations. Exp. Mech. 55 (1), 261–274.

Bennour, Z., Ishida, T., Nagaya, Y., Chen, Y., Nara, Y., Chen, Q., Sekine, K., Nagano, Y., 2015. Crack extension in hydraulic fracturing of shale cores using viscous oil, water, and liquid carbon dioxide. Rock Mech. Rock Eng. 48 (4), 1463–1473.

Birdwell, J.E., Mercier, T.J., Johnson, R.C., Brownfield, M.E., 2013. In-place Oil Shale Resources Examined by Grade in the Major Basins of the Green River Formation, Colorado, Utah, and Wyoming. US Department of the Interior, US Geological Survey.

Burnham, A.K., 2018. Thermomechanical properties of the Garden Gulch member of the green river formation. Fuel 219, 477–491.

Burnham, A.K., McConaghy, J.R., 2014. Semi-open pyrolysis of oil shale from the Garden Gulch member of the green river formation. Energy Fuels 28 (12), 7426–7439.

Chen, Y., Naoi, M., Tomonaga, Y., Akai, T., Tanaka, H., Takagi, S., Ishida, T., 2018. Method for visualizing fractures induced by laboratory-based hydraulic fracturing and its application to shale samples. Energies 11 (8), 1976.

Chen, Hao, Hu, Yi, Kang, Yong, Cai, Can, Liu, Jiawei, Liu, Yiwei, 2019. Fracture initiation and propagation under different perforation orientation angles in supercritical CO₂ fracturing. J. Petrol. Sci. Eng. 183, 106403.

Cheng, G., Deng, B., Liu, Y., Chen, J., Wang, K., Zhang, D., Li, M., 2020. Experimental investigation on the feasibility and efficiency of shear-fracturing stimulation for enhancing coal seam permeability. J. Nat. Gas Sci. Eng. 103381.

Closmann, P., Bradley, W., et al., 1979. The effect of temperature on tensile and compressive strengths and Young's modulus of oil shale. Soc. Petrol. Eng. J. 19 (5), 301–312.

Culp, B.M., 2014. Impact of Co2 on Fracture Complexity when Used as a Fracture Fluid in Rock.

Dyni, J.R., et al., 2006. Geology and Resources of Some World Oil-Shale Deposits.

Edelman, E., Burghardt, J., McPherson, B., et al., 2018. Experimental investigation of time-dependent deformation of fluid disposal reservoir caprocks. In: 52nd US Rock Mechanics/Geomechanics Symposium. American Rock Mechanics Association.

Gandossi, L., et al., 2013. An overview of hydraulic fracturing and other formation stimulation technologies for shale gas production. Eur. Commisson Jt. Res. Cent. Tech. Reports 26347.

Gdoutos, E.E., 2012. Fracture Mechanics Criteria and Applications, vol. 10. Springer Science & Business Media.

Germanovich, L.N., Astakhov, D.K., Mayerhofer, M.J., Shlyapobersky, J., Ring, L.M., 1997. Hydraulic fracture with multiple segments i. observations and model formulation. Int. J. Rock Mech. Min. Sci. 34 (3–4), 97–e1.

Ghaboussi, J., Pecknold, D.A., Wu, X.S., 2017. Nonlinear Computational Solid Mechanics. CRC Press.

Glatz, G., Lapene, A., Castanier, L.M., Kovscek, A.R., 2018. An experimental platform for triaxial high-pressure/high-temperature testing of rocks using computed tomography. Rev. Sci. Instrum. 89 (4), 045101.

Guo, F., Morgenstern, N., Scott, J., 1993. Interpretation of hydraulic fracturing breakdown pressure. In: International Journal of Rock Mechanics and Mining Sciences & Geomechanics Abstracts, vol. 30. Elsevier, pp. 617–626.

Haimson, B., Fairhurst, C., et al., 1967. Initiation and extension of hydraulic fractures in rocks. Soc. Petrol. Eng. J. 7 (3), 310–318.

Huang, Xianfu, Zhao, Ya-Pu, Wang, Xiaohe, Pan, Lisheng, 2019. Adsorption-induced pore blocking and its mechanisms in nanoporous shale due to interactions with supercritical CO_2. J. Petrol. Sci. Eng. 178, 74–81.

Hubbert, M.K., Willis, D.G., 1972. Mechanics of Hydraulic Fracturing.

Jackson, R.B., Vengosh, A., Carey, J.W., Davies, R.J., Darrah, T.H., O'sullivan, F., Pétron, G., 2014. The environmental costs and benefits of fracking. Annu. Rev. Environ. Resour. 39, 327–362.

Jew, A.D., Dustin, M.K., Harrison, A.L., Joe-Wong, C.M., Thomas, D.L., Maher, K., Brown Jr., G.E., Bargar, J.R., 2017. Impact of organics and carbonates on the oxidation and precipitation of iron during hydraulic fracturing of shale. Energy Fuels 31 (4), 3643–3658.

Jiang, Y., Qin, C., Kang, Z., Zhou, J., Li, Y., Liu, H., Song, X., 2018. Experimental study of supercritical CO2 fracturing on initiation pressure and fracture propagation in shale under different triaxial stress conditions. J. Nat. Gas Sci. Eng. 55, 382–394.

Kim, T.W., Ross, C.M., Guan, K.M., Burnham, A.K., Kovscek, A.R., et al., 2020a. Permeability and porosity evolution of organic-rich shales from the Green River Formation as a result of maturation. SPE Journal 25 (3). SPE-195366-PA.

Kim, T.W., Yun, W., Kovscek, A.R., 2020b. Application of Digital Volume Correlation to X-ray Computed Tomography Images of Shale. Energy Fuel 34 (11), 13636–13649.

Kizaki, A., Tanaka, H., Ohashi, K., Sakaguchi, K., Matsuki, K., et al., 2012. Hydraulic fracturing in inada granite and ogino tuff with super critical carbon dioxide. In: ISRM Regional Symposium-7th Asian Rock Mechanics Symposium. International Society for Rock Mechanics.

Lai, W.M., Rubin, D.H., Krempl, E., Rubin, D., 2009. Introduction to Continuum Mechanics. Butterworth-Heinemann.

Li, X., Feng, Z., Han, G., Elsworth, D., Marone, C., Saffer, D., Cheon, D.S., 2016. Breakdown pressure and fracture surface morphology of hydraulic fracturing in shale with H2O, CO2 and N2. Geomechanics and Geophysics for Geo-Energy and Geo-Resources 2 (2), 63–76.

Lu, Yiyu, Ao, Xiang, Tang, Jiren, Jia, Yunzhong, Zhang, Xinwei, Chen, Yuting, 2016. Swelling of shale in supercritical carbon dioxide. J. Nat. Gas Sci. Eng. 30, 268–275.

Lubinski, A., 1954. The theory of elasticity for porous bodies displaying a strong pore structure. SAVE Proc. 247–256.

Lyu, Qiao, Long, Xinping, Ranjith, P.G., Tan, Jingqiang, Kang, Yong, Wang, Zhanghu, 2018. Experimental investigation on the mechanical properties of a low-clay shale with different adsorption times in sub-/super-critical CO2. Energy 147, 1288–1298.

Morita, N., Black, A., Guh, G., et al., 1990. Theory of lost circulation pressure. In: SPE Annual Technical Conference and Exhibition. Society of Petroleum Engineers.

Petrie, E.S., Evans, J.P., Bauer, S., 2014. Failure of cap-rock seals as determined from mechanical stratigraphy, stress history, and tensile-failure analysis of exhumed analogsstress history and tensile failure analysis of exhumed caprock seal analogs. AAPG (Am. Assoc. Pet. Geol.) Bull. 98 (11), 2365–2389.

Rogala, A., Krzysiek, J., Bernaciak, M., Hupka, J., 2013. Non-aqueous fracturing technologies for shale gas recovery. Physicochemical Problems of Mineral Processing 49.

Rummel, F., 1987. Fracture mechanics approach to hydraul c fracturing stress measurements. Fracture mechanics of rock 217.

Shainberg, I., Letey, J., et al., 1984. Response of soils to sodic and saline conditions. Hilgardia 52 (2), 1–57.

Stanisławek, S., Kędzierski, P., Miedzińska, D., 2017. Laboratory hydraulic fracturing tests of rock samples with water, carbon dioxide, and slickwater. Arch. Civ. Eng. 63 (3), 139–148.

Stock, J., Healy, J., Hickman, S., Zoback, M., 1985. Hydraulic fracturing stress measurements at Yucca Mountain, Nevada, and relationship to the regional stress field. J. Geophys. Res.: Solid Earth 90 (B10), 8691–8706.

Tomac, I., Gutierrez, M., 2017. Coupled hydro-thermo-mechanical modeling of hydraulic fracturing in quasi-brittle rocks using bpm-dem. Journal of Rock Mechanics and Geotechnical Engineering 9 (1), 92–104.

Upadhyaya, S., 2005. Stress–strain and Soil Strength.

Vega, B., Dutta, A., Kovscek, A.R., 2014. Ct imaging of low-permeability, dual-porosity systems using high x-ray contrast gas. Transport Porous Media 101 (1), 81–97.

Wang, H., 2015. Numerical modeling of non-planar hydraulic fracture propagation in brittle and ductile rocks using X-FEM with cohesive zone method. J. Petrol. Sci. Eng. 135, 127–140.

White, J.A., Burnham, A.K., Camp, D.W., 2017. A thermoplasticity model for oil shale. Rock Mech. Rock Eng. 50 (3), 677–688.

Yu, W., Lashgari, H.R., Wu, K., Sepehrnoori, K., 2015. CO2 injection for enhanced oil recovery in bakken tight oil reservoirs. Fuel 159, 354–363.

Zhang, X., Lu, Y., Tang, J., Zhou, Z., Liao, Y., 2017. Experimental study on fracture initiation and propagation in shale using supercritical carbon dioxide fracturing. Fuel 190, 370–378.

Zhang, Yixiang, He, Jianming, Li, Xiao, Lin, Chong, 2019. Experimental study on the supercritical CO2 fracturing of shale considering anisotropic effects. J. Petrol. Sci. Eng. 173, 932–940.

Zoback, M., Rummel, F., Jung, R., Raleigh, C., 1977. Laboratory hydraulic fracturing experiments in intact and pre-fractured rock. In: International Journal of Rock Mechanics and Mining Sciences & Geomechanics Abstracts, vol. 14. Elsevier, pp. 49–58.

Zou, Y., Li, N., Ma, X., Zhang, S., Li, S., 2018. Experimental study on the growth behavior of supercritical CO2-induced fractures in a layered tight sandstone formation. J. Nat. Gas Sci. Eng. 49, 145–156.